A NEW TECHNIQUE FOR SIMULATING COMPOSITE MATERIAL

Task 2: Analytical Solutions with Generalized Impedance Boundary Conditions (GIBCs)

Period: September 1989 - February 1990

The Radiation Laboratory
Department of Electrical Engineering
and Computer Science
The University of Michigan
Ann Arbor, MI 48109-2122

National Aeronautics and
Space Administration
Ames Research Center
Moffett Field, CA 94035
Grant NAG-2-541

UM Report #025921-8-T

Technical Report for NASA Grant NAG-2-541

NASA Technical Monitor: Alex Woo

Grant Title: A NEW TECHNIQUE FOR SIMULATING COMPOSITE MATERIAL
Task 2: Analytical Solutions with Generalized Impedance Boundary Conditions (GIBCs)

Institution: The Radiation Laboratory
Department of Electrical Engineering
and Computer Science
The University of Michigan
Ann Arbor, Michigan 48109-2122

Period Covered: September 1989 - February 1990

Report Title: Diffraction by a Multilayer Slab Recessed in a Ground Plane via Generalized Impedance Boundary Conditions

Report Authors: M. A. Ricoy and J. L. Volakis

Principal Investigator: John L. Volakis
Telephone: (313) 764-0500

Diffraction by a Multilayer Slab Recessed in a Ground Plane via Generalized Impedance Boundary Conditions [1]

December, 1989

M. A. Ricoy and J. L. Volakis

Radiation Laboratory

Department of Electrical Engineering and Computer Science

The University of Michigan

Ann Arbor, Michigan 48109-2122

Abstract-The diffraction problem associated with a multilayer material slab recessed in a perfectly conducting ground plane is formulated and solved via the Generalized Scattering Matrix Formulation (GSMF) in conjunction with the dual integral equation approach. The multilayer slab is replaced by a surface obeying a generalized impedance boundary condition (GIBC) to facilitate the computation of the pertinent Wiener Hopf split functions and their zeros. Both E_z and H_z polarizations are considered and a number of scattering patterns are presented, some of which are compared to exact results available for a homogeneous recessed slab.

Contents

1 Introduction

More sophisticated fabrication techniques and design methodologies have lead to a greater utilization of microstrip antenna devices with multilayer substrates. When these appear on airborne vehicles (e.g., as part of a flush-mounted antenna configuration), their scattering properties become important.

The scattering of a microstrip configuration may in general be understood through a characterization of the scattering substructures which comprise it. In this paper we investigate the plane wave diffraction from one such substructure, the multilayer semi-infinite slab recessed in a perfectly conducting ground plane (figure 1a). To the authors' knowledge, this problem has not yet been attempted. However, several researchers have considered the special case where the slab is homogeneous [*Pathak*, 1979; *Volakis and Ricoy*, 1989; *Ricoy and Volakis*, 1989a]. A common feature of these analyses, though, is a requirement to solve for the fields internal to the dielectric, making them cumbersome and impractical to implement in the case of the multilayered slab.

The difficulty in working with the internal fields is alleviated here-in by representing the multilayer slab as a surface characterized by a plane wave reflection coefficient $R(\cos\phi_o)$ (see figure 1b), where ϕ_o can be extended through analytic continuation in the complex plane. This enables us to carry out the analysis in a symbolic manner regardless of the inhomogeneity profile of the layer. Hence, although our focus in this paper is the multilayer recessed slab, the derivations will be applicable to any vertically inhomogeneous slab.

The problem herein is formulated via the dual integral equation approach [*Clem-*

mow, 1951] in conjunction with the generalized scattering matrix formulation (GSMF) [*Pace and Mittra*, 1964]. The GSMF is applied to the recessed stub structure of figure 2a, depicting a perfeclty conducting half plane elevated a distance δ above a reflecting surface with a perfectly conducting stub recessed a distance d away from the half plane edge. This formulation requires the solution to a number of individual subproblems. As illustrated in figures 2b-f, they correspond to the problems of direct diffraction, mode coupling, mode reflection, and mode radiation. Once solutions to each of these subproblems have been obtained via the dual integral equation method, they can be combined in accordance with the GSMF prescription to yield the diffraction for the original structure in figure 1a.

Unfortunately, the conversion of the symbolic solution into one of practical use proves to be a formidable task when the reflection coefficient of the grounded slab is obtained in its exact form. The fundamental difficulties are related to:

- the factorization or splitting of the associated Wiener Hopf functions into components regular in the upper and lower half complex plane, and
- the extraction of the complex zeros (i.e., the waveguide modes) associated with the split functions.

The pertinent Wiener Hopf functions cannot be factored analytically and one must therefore resort to a numerical scheme (e.g., see *Ricoy and Volakis* [1989a]). Also, in solving for the complex roots of the pertinent split functions, it is necessary to employ a search algorithm in the complex plane, a process which is numerically intensive. We circumvent these difficulties by replacing the grounded slab by an

opaque sheet satisfying a generalized impedance boundary condition (GIBC) [*Karp and Karal*, 1965]. The GIBCs involve higher order derivatives of the normal surface fields and reduce to the standard impedance boundary condition when only the first normal derivative of the field is kept. They have been shown to provide accurate simulations of thick coatings and in general their accuracy is analogous to the order to the condition (equal to the highest derivative retained). Their derivation has been discussed in *Rojas and Al-hekail* [1989], *Senior and Volakis* [1989], *Bernard* [1987], *Volakis and Senior* [1989], *Volakis and Syed* [1989] and *Ricoy and Volakis* [1989b], and amounts to the specification of the constants multiplying the field derivatives so that the impedance sheet simulation of the grounded slab yields a reflection coefficient that best approximates the corresponding exact one. This approximate reflection coefficient is cast as a ratio of polynomials in $\cos\phi$ or $\sin\phi$, making the determination of the complex poles and zeros of the reflection coefficient a simple task. As a result, the required Wiener Hopf factorizations can be obtained analytically leading to computationally efficient solutions.

In the first part of the paper we summarize the GSMF procedure. The dual integral equation method is subsequently employed to formulate each of the subproblems and the necessary solutions are obtained for both E_z and H_z polarizations. These are given in terms of symbolic split functions which are then evaluated for the specific case of a multilayer grounded slab by casting the reflection coefficient in a form compatible with a GIBC simulation of the slab [*Ricoy and Volakis*, 1989b]. Results are given and the accuracy of the GIBC simulation is examined by comparison with known results for homogeneous slabs.

2 Description of GSMF Procedure

In this section, the generalized scattering matrix formulation (GSMF) is applied to the geometry given in figure 2a. This consists of a perfectly conducting half-plane located a distance δ above the grounded slab, with a perfectly conducting stub recessed a distance d away from the half-plane edge. To concurrently treat both the E_z and H_z polarizations of incidence, the quantities F_z and F_x are introduced. They are defined as

$$F_z = \begin{cases} E_z, & E_z \text{ polarization,} \\ Z_o H_z, & H_z \text{ polarization.} \end{cases} \tag{1}$$

$$F_x = \begin{cases} Z_o H_x, & E_z \text{ polarization,} \\ E_x, & H_z \text{ polarization.} \end{cases} \tag{2}$$

and from Maxwell's equations

$$F_x = -\frac{jv_1}{k}\frac{\partial F_z}{\partial y} \tag{3}$$

where

$$v_1 = \begin{cases} -1, & E_z \text{ polarization,} \\ 1, & H_z \text{ polarization.} \end{cases} \tag{4}$$

The individual problems to be considered in the GSMF prescription [*Pace and Mittra*, 1964] are as follows:

1. Evaluation of the direct diffracted field by the substructure in figure 2b due to a plane wave incidence. This field can be expressed as

$$F_z^{dd}(\phi, \phi_o) = \int_C P_{dd}(\cos\alpha, \cos\phi_o; \delta)\, e^{-jk_o\rho\cos(\alpha-\phi)} d\alpha \tag{5}$$

where P_{dd} is the spectrum associated with the currents induced on the half plane and (ρ, ϕ) are the usual cylindrical coordinates of the observation point.

Additionally, C is the complex contour composed of the directed line segments $[0-j\infty, 0-j0], [0-j0, \pi-j0], [\pi-j0, \pi+j\infty]$ in the complex α plane.

2. Evaluation of the field coupled into the waveguide due to a plane wave incidence (figure 2c) as illustrated. We denote the field corresponding to the n^{th} coupled mode as

$$F^c_{zn}(\phi_o) = C_n(\cos\phi_o; \delta)\, e^{-jk_n x} \tag{6}$$

where $C_n(\cos\phi_o; \delta)$ is usually referred to as the coupling coefficient and k_n is the propagation constant associated with the n^{th} mode.

3. Evaluation of the modal field reflected at the stub (figure 2d). This can be expressed as $\Gamma_{mn} e^{jk_m x}$ where Γ_{mn} is the stub reflection coefficient of the n^{th} mode to the m^{th} mode.

4. Evaluation of the reflected field at the waveguide mouth due to the n^{th} mode (figure 2e). This can be expressed by $R_{mn}(\delta)\, e^{-jk_m x}$ where $R_{mn}(\delta)$ is the reflection coefficient of the n^{th} mode to the m^{th} mode.

5. Evaluation of the radiated field attributed to the m^{th} mode incident at the waveguide mouth (figure 2f). This field can be expressed as

$$F^l_{zm}(\phi) = \int_C P_m(\cos\alpha; \delta)\, e^{-jk_o\rho\cos(\alpha-\phi)} d\alpha \tag{7}$$

where $P_m(\cos\alpha, \delta)$ is proportional to the spectrum of the currents induced on the half plane due to the incident m^{th} mode.

Accordingly, the scattered field by the recessed stub geometry in figure 2a is given by

$$F_z^s(\phi,\phi_o,\delta,d)=\int_C\left[P_{dd}(\cos\alpha,\cos\phi_o;\delta)+P_{mod}(\cos\alpha,\cos\phi_o;\delta,d)\right]e^{-jk_o\rho\cos(\alpha-\phi)}d\alpha\ ;\ y>\delta \tag{8}$$

where $P_{mod}(\cos\alpha,\cos\phi_o;\delta,d)$ is associated with the presence of the stub and includes the contribution of the waveguide modal fields. It can be written in a matrix form as [*Pace and Mittra*, 1964]

$$\begin{aligned}P_{mod}(\cos\alpha,\cos\phi_o;\delta,d) &= [P_m(\cos\alpha;\delta)]^T\{[I]-[W_{mn}(d)][\Gamma_{mn}][W_{mn}(d)][R_{mn}(\delta)]\}^{-1}\\ &\quad\cdot[W_{mn}(d)][\Gamma_{mn}][W_{mn}(d)][C_n(\cos\phi_o;\delta)]\end{aligned} \tag{9}$$

in which the brackets signify column or square matrices depending on whether one or two subscripts appear, respectively. In addition, $[I]$ denotes the identity matrix and $[W_{mn}(d)]$ is the modal propagation matrix whose elements are given by

$$W_{mn}(d)=\begin{cases}e^{-jk_nd}, & m=n\\ 0, & m\neq n.\end{cases} \tag{10}$$

To obtain the field scattered by the recessed material slab it is only required to set d and δ to 0 in (8) and (9). In this case, $[W_{mn}(d=0)]$ becomes the identity matrix and $[\Gamma_{mn}]$ reduces to $[I]$ or $-[I]$ for H_z and E_z polarizations, respectively. Thus, P_{mod} becomes

$$\begin{aligned}P_{mod}(\cos\alpha,\cos\phi_o) &\stackrel{def}{=} P_{mod}(\cos\alpha,\cos\phi_o;\delta=0,d=0)\\ &= [P_m(\cos\alpha)]\{[I]-v_1[R_{mn}]\}^{-1}[v_1C_n(\cos\phi_o)]\end{aligned} \tag{11}$$

where

$$P_m(\cos\alpha)\stackrel{def}{=}P_m(\cos\alpha;\delta=0)$$

$$C_n(\cos\phi_o) \stackrel{def}{=} C_n(\cos\phi_o; \delta = 0)$$
$$R_{mn} \stackrel{def}{=} R_{mn}(\delta = 0). \tag{12}$$

Hence, the field scattered by the vertically inhomogeneous recessed slab can be expressed as

$$F_z^s(\phi, \phi_o) = \int_C P_{rs}(\cos\alpha, \cos\phi_o)\, e^{-jk_o\rho\cos(\alpha-\phi)} d\alpha \; ; \; y > 0 \tag{13}$$

where

$$P_{rs}(\cos\alpha, \cos\phi_o) = P_{dd}(\cos\alpha, \cos\phi_o) + P_{mod}(\cos\alpha, \cos\phi_o). \tag{14}$$

The steepest descent method can then be employed to evaluate (13) and obtain the diffracted field.

3 Plane Wave Diffraction and Mode Coupling

Consider the plane wave

$$F_z^i = e^{jk_o(x\cos\phi_o + y\sin\phi_o)} \tag{15}$$
$$F_x^i = v_1 \sin\phi_o e^{jk_o(x\cos\phi_o + y\sin\phi_o)} \tag{16}$$

incident at an angle ϕ_o upon the structure depicted in figure 2b. In the absence of the perfectly conducting half-plane, the total fields may be written as (for $y > 0$)

$$F_z^{pw} = F_z^i + F_z^r \tag{17}$$
$$F_x^{pw} = F_x^i + F_x^r \tag{18}$$

with

$$F_z^r = R(\cos\phi_o)\, e^{jk_o(x\cos\phi_o - y\sin\phi_o)} \tag{19}$$
$$F_x^r = -v_1 R(\cos\phi_o) \sin\phi_o e^{jk_o(x\cos\phi_o - y\sin\phi_o)} \tag{20}$$

where $R(\cos\phi_o)$ denotes the plane wave reflection coefficient of the grounded slab referred to $y = 0$. For the general case of a plane wave incident at an angle α on a vertically inhomogeneous ground plane coating, $R(\lambda = \cos\alpha)$ may be represented as

$$R(\lambda) = -\left[\frac{A(\lambda) - \sqrt{1-\lambda^2}B(\lambda)}{A(\lambda) + \sqrt{1-\lambda^2}B(\lambda)}\right], \tag{21}$$

where $A(\lambda)$ and $B(\lambda)$ are even functions of λ, with any branch cuts in $A(\lambda)$ also appearing in $B(\lambda)$ and vice versa.

The introduction of the perfectly conducting half plane at $y = \delta$ generates an additional scattered field component F_z^s so that the total fields become

$$F_z = F_z^{pw} + F_z^s \tag{22}$$

$$F_x = F_x^{pw} + F_x^s \tag{23}$$

This scattered field is due to induced currents on the perfectly conducting half plane, and can thus be represented by an angular spectrum of plane waves. A suitable representation is [*Clemmow*, 1951]

$$F_z^s = \begin{cases} \int_C P(\cos\alpha)\, e^{jk_o\delta\sin\alpha} e^{-jk_o\rho\cos(\phi-\alpha)} d\alpha & y > \delta, \\ \int_C Q(\cos\alpha)\, e^{-jk_o\delta\sin\alpha}\left[e^{-jk_o\rho\cos(\phi+\alpha)} + R(\cos(\pi-\alpha))\, e^{-jk_o\rho\cos(\phi-\alpha)}\right] d\alpha & 0 < y < \delta, \end{cases} \tag{24}$$

implying

$$F_x^s = \begin{cases} -\int_C v_1 \sin\alpha\, P(\cos\alpha)\, e^{jk_o\delta\sin\alpha} e^{-jk_o\rho\cos(\phi-\alpha)} d\alpha & y > \delta, \\ \int_C v_1 \sin\alpha\, Q(\cos\alpha)\, e^{-jk_o\delta\sin\alpha}\left[e^{-jk_o\rho\cos(\phi+\alpha)} - R(\cos(\pi-\alpha))\, e^{-jk_o\rho\cos(\phi-\alpha)}\right] d\alpha & 0 < y < \delta \end{cases} \tag{25}$$

in which $P(\cos\alpha)$ and $Q(\cos\alpha)$ are the unknown spectral functions to be determined from the boundary conditions at $y = 0$. These are

(B1) Continuity of the tangential electric fields at $y = \delta$, $-\infty < x < \infty$

(B2) Continuity of the tangential magnetic fields at $y = \delta$, $x < 0$ and

(B3) Vanishing tangential electric field on the perfectly conducting half plane at $y = \delta$, $x > 0$

and we note that the boundary condition at the slab surface is implicitly taken into account by the representation (24) and (25).

The application of (B1)-(B3) in conjunction with (24) and (25) is straightforward. It results in the set of equations

$$P(\lambda) = -v_1 Q(\lambda)\left[1 - v_1 R(\lambda)\, e^{-j2k_o\delta\sqrt{1-\lambda^2}}\right]. \tag{26}$$

$$\int_{-\infty}^{\infty} Q(\lambda)\, v_2(\lambda)\, e^{-jk_o x\lambda} d\lambda = 0 \quad ; \quad x < 0, \tag{27}$$

$$\int_{-\infty}^{\infty} Q(\lambda)\, v_3(\lambda)\left[1 - v_1 R(\lambda)\, e^{-2jk_o\delta\sqrt{1-\lambda^2}}\right] e^{-jk_o x\lambda} d\lambda =$$
$$-v_3(\lambda_o)\sqrt{1-\lambda_o^2}\, e^{jk_o\delta\sqrt{1-\lambda_o^2}}\left[1 - v_1 R(\lambda_o)\, e^{-2jk_o\delta\sqrt{1-\lambda_o^2}}\right] e^{jk_o x\lambda_o} \quad ; \quad x > 0 \tag{28}$$

where we have set $\lambda = \cos\alpha$, $\lambda_o = \cos\phi_o$ and

$$v_2(\lambda) = \begin{cases} 1, & E_z \text{ polarization}, \\ 1/\sqrt{1-\lambda^2}, & H_z \text{ polarization}. \end{cases} \tag{29}$$

$$v_3(\lambda) = \begin{cases} 1/\sqrt{1-\lambda^2}, & E_z \text{ polarization}, \\ 1, & H_z \text{ polarization}. \end{cases} \tag{30}$$

These are sufficient to obtain a solution for $Q(\lambda)$ and $P(\lambda)$. However, before proceeding, it is necessary to rewrite certain terms in the integrands of (27) and (28) as products of "upper" and "lower" functions, that is, functions free of poles, zeros, and branch cuts in the upper and lower half λ planes, respectively. In the

process of doing so, we introduce the definitions

$$v_2(\lambda) \stackrel{def}{=} v_2^+(\lambda)\, v_2^-(\lambda) \tag{31}$$

$$v_3(\lambda) \stackrel{def}{=} v_3^+(\lambda)\, v_3^-(\lambda) \tag{32}$$

$$1 - v_1 R(\lambda)\, e^{-2jk_o\delta\sqrt{1-\lambda^2}} \stackrel{def}{=} \frac{L_w(\lambda;\delta)\, U_w(\lambda;\delta)}{L_s(\lambda)\, U_s(\lambda)}, \tag{33}$$

in which

$$L_w(\lambda;\delta)\, U_w(\lambda;\delta) = A(\lambda)\left(1 + v_1\, e^{-2jk_o\delta\sqrt{1-\lambda^2}}\right) + \sqrt{1-\lambda^2}B(\lambda)\left(1 - v_1\, e^{-2jk_o\delta\sqrt{1-\lambda^2}}\right) \tag{34}$$

$$L_s(\lambda)\, U_s(\lambda) = A(\lambda) + \sqrt{1-\lambda^2}B(\lambda). \tag{35}$$

In these, $L_s(\lambda)$, $L_w(\lambda;\delta)$, $v_2^-(\lambda)$, $v_3^-(\lambda)$ are lower functions while $U_s(\lambda)$,$U_w(\lambda;\delta)$, $v_2^+(\lambda)$, $v_3^+(\lambda)$ denote upper functions. We also note that L_wU_w is a function characteristic to the loaded parallel plate waveguide and its zeros correspond to modes in the waveguide. On the other hand, L_sU_s is a function characteristic to the grounded slab with its zeros corresponding to the surface wave modes supported by the slab.

Substituting (31)-(35) into (27) and (28), we have

$$\int_{-\infty}^{\infty} Q(\lambda)\, v_2^+(\lambda)\, v_2^-(\lambda)\, e^{-jk_ox\lambda} d\lambda = 0 \quad ; \quad x < 0, \tag{36}$$

$$\int_{-\infty}^{\infty} Q(\lambda)\, v_3^+(\lambda)\, v_3^-(\lambda)\, \frac{L_w(\lambda;\delta)\, U_w(\lambda;\delta)}{L_s(\lambda)\, U_s(\lambda)} e^{-jk_ox\lambda} d\lambda =$$

$$-v_3^+(\lambda_o)\, v_3^-(\lambda_o)\sqrt{1-\lambda_o^2}\, e^{jk_o\delta\sqrt{1-\lambda_o^2}} \frac{L_w(\lambda_o;\delta)\, U_w(\lambda_o;\delta)}{L_s(\lambda_o)\, U_s(\lambda_o)} e^{jk_ox\lambda_o} \quad ; \quad x > 0 \tag{37}$$

These coupled dual integral equations can be solved for the unknown spectra by examining the analytic properties of the integrands, and the reader is referred to *Clemmow* [1951] and *Ricoy and Volakis* [1989a] for a more explicit description of

this process. From (36) and (37) the unknown spectra are determined to be

$$Q(\lambda) = \frac{L_w(\lambda_o;\delta)\,U_s(\lambda)}{2\pi j U_w(\lambda;\delta)\,L_s(\lambda_o)}\left[\frac{v_2^+(\lambda_o)\,v_3^-(\lambda_o)\sqrt{1-\lambda_o^2}}{v_2^-(\lambda)\,v_3^+(\lambda)\,(\lambda+\lambda_o)}\right] e^{jk_o\delta\sqrt{1-\lambda_o^2}} \tag{38}$$

$$P(\lambda) = \frac{-v_1 L_w(\lambda;\delta)\,L_w(\lambda_o;\delta)}{2\pi j L_s(\lambda)\,L_s(\lambda_o)}\left[\frac{v_2^+(\lambda_o)\,v_3^-(\lambda_o)\sqrt{1-\lambda_o^2}}{v_2^-(\lambda)\,v_3^+(\lambda)\,(\lambda+\lambda_o)}\right] e^{jk_o\delta\sqrt{1-\lambda_o^2}}. \tag{39}$$

Recognizing that $P_{dd}(\lambda) = P(\lambda)$, we may then set $\delta = 0$ and substitute for the polarization dependent functions to obtain

$$P_{dd}^e(\lambda) = \frac{L_w(\lambda)\,L_w(\lambda_o)}{2\pi j L_s(\lambda)\,L_s(\lambda_o)}\frac{\sqrt{1-\lambda}\sqrt{1-\lambda_o}}{(\lambda+\lambda_o)} \tag{40}$$

$$P_{dd}^h(\lambda) = -\frac{L_w(\lambda)\,L_w(\lambda_o)}{2\pi j L_s(\lambda)\,L_s(\lambda_o)}\frac{\sqrt{1+\lambda}\sqrt{1+\lambda_o}}{(\lambda+\lambda_o)} \tag{41}$$

where the superscripts e and h refer to the spectra associated with E_z and H_z polarizations, respectively.

To solve for the field coupled into the region $0 < y < \delta$, $x > 0$, (21), (33) and (38) are substituted into (24) to obtain the integral expression

$$F_z^s = \int_{-\infty}^{\infty} \frac{v_2^+(\lambda_o)\,v_3^-(\lambda_o)\sqrt{1-\lambda_o^2}}{2\pi j v_2^-(\lambda)\,v_3^+(\lambda)\,(\lambda+\lambda_o)} \frac{L_w(\lambda_o;\delta)\,e^{jk_o\delta\left[\sqrt{1-\lambda_o^2}-\sqrt{1-\lambda^2}\right]}}{L_s(\lambda_o)\,L_s(\lambda)\,U_w(\lambda;\delta)}$$
$$\cdot\left[2jA(\lambda)\frac{\sin\left(ky\sqrt{1-\lambda^2}\right)}{\sqrt{1-\lambda^2}} + 2B(\lambda)\cos\left(k_o y\sqrt{1-\lambda^2}\right)\right] e^{-jkx\lambda}d\lambda \quad ;0 < y < \delta \tag{42}$$

This can be evaluated by closing the path of integration via a semi-infinite contour in the lower-half λ-plane. The sum of the residues of the captured poles then yields

$$F_z^s = \sum_{n=1}^{N} C_n(\lambda_o)\left\{jA(\lambda_n)\frac{\sin\left(k_o y\sqrt{1-\lambda_n^2}\right)}{\sqrt{1-\lambda_n^2}} + B(\lambda_n)\cos\left(k_o y\sqrt{1-\lambda_n^2}\right)\right\} e^{-jk_o x\lambda_n} \tag{43}$$

where $\{\lambda_n\}$ are the zeros of $U_w(\lambda;\delta)$,

$$C_n(\lambda_o) = -2\,e^{jk_o\delta\sqrt{1-\lambda_o^2}-\sqrt{1-\lambda_n^2}}\frac{L_w(\lambda_o;\delta)}{L_s(\lambda_n)\,L_s(\lambda_o)\,U_w'(\lambda_n;\delta)}\frac{v_2^+(\lambda_o)\,v_3^-(\lambda_o)\sqrt{1-\lambda_o^2}}{v_2^-(\lambda_n)\,v_3^+(\lambda_n)\,(\lambda_n+\lambda_o)}, \tag{44}$$

and

$$U_w'(\lambda_n;\delta) = \left.\frac{dU_w}{d\lambda}\right|_{\lambda=\lambda_n}. \tag{45}$$

Substituting (29) and (30) into (44) with $\delta = 0$, we obtain the more explicit forms for $C_n(\lambda_o)$ as

$$C_n^e(\lambda_o) = -\frac{2L_w(\lambda_o)}{L_s(\lambda_n)\,L_s(\lambda_o)\,U_w'(\lambda_n)}\frac{\sqrt{1-\lambda_o}\sqrt{1-\lambda_n}}{\lambda_o+\lambda_n} \tag{46}$$

$$C_n^h(\lambda_o) = -\frac{2L_w(\lambda_o)}{L_s(\lambda_n)\,L_s(\lambda_o)\,U_w'(\lambda_n)}\frac{\sqrt{1+\lambda_o}\sqrt{1+\lambda_n}}{\lambda_o+\lambda_n} \tag{47}$$

for E_z and H_z polarizations, respectively.

4 Reflection and Launching of a Waveguide Mode

Consider now then n^{th} waveguide mode field

$$\begin{cases} F_{zn} = \left[jA(\lambda_n)\dfrac{\sin\left(k_oy\sqrt{1-\lambda_n^2}\right)}{\sqrt{1-\lambda_n^2}} + B(\lambda_n)\cos\left(k_oy\sqrt{1-\lambda_n^2}\right)\right]e^{jk_ox\lambda_n} \\ F_{xn} = \left[v_1A(\lambda_n)\cos\left(k_oy\sqrt{1-\lambda_n^2}\right) + jv_1B(\lambda_n)\sqrt{1-\lambda_n^2}\sin\left(k_oy\sqrt{1-\lambda_n^2}\right)\right]e^{jk_ox\lambda_n} \end{cases} \quad 0<y<\delta \tag{48}$$

incident at the waveguide opening (figure 2e). The radiated fields due to this excitation may be again represented by (24) - (25). Subsequent application of the boundary conditions (B1)-(B3) then yields the dual integral equations (with the usual transformation to the λ plane)

$$\int_{-\infty}^{\infty} Q(\lambda)\,v_3^+(\lambda)\,v_3^-(\lambda)\frac{L_w(\lambda;\delta)\,U_w(\lambda;\delta)}{L_s(\lambda)\,U_s(\lambda)}e^{-jk_ox\lambda}d\lambda = 0 \;\;;\;\; x>0 \tag{49}$$

$$\int_{-\infty}^{\infty} Q(\lambda)\, v_2^+(\lambda)\, v_2^-(\lambda)\, e^{-jk_o x\lambda} d\lambda \;=\; \frac{-v_4 e^{jk_o x\lambda_n}}{2\cos\left(k_o\delta\sqrt{1-\lambda_n^2}\right)} \quad ;\quad x < 0 \tag{50}$$

where

$$v_4 = \begin{cases} A(\lambda_n) & , E_z \text{ polarization} \\ B(\lambda_n) & , H_z \text{ polarization.} \end{cases} \tag{51}$$

The solution of those proceeds in a manner parallel to the previous case. The resulting spectra are determined to be

$$Q(\lambda) \;=\; \frac{-v_4 L_w(\lambda_n) U_s(\lambda)\, v_3^-(\lambda_n)}{4\pi j\cos\left(k_o\delta\sqrt{1-\lambda_n^2}\right) L_s(\lambda_n) U_w(\lambda;\delta)\, v_2^-(\lambda)\, v_2^-(\lambda_n)\, v_3^+(\lambda)\,(\lambda+\lambda_n)} \tag{52}$$

$$P(\lambda) \;=\; \frac{v_1 v_4 L_w(\lambda_n) L_w(\lambda;\delta)(\lambda_n)\, v_3^-(\lambda_n)}{4\pi j\cos\left(k_o\delta\sqrt{1-\lambda_n^2}\right) L_s(\lambda_n) L_s(\lambda)\, v_2^-(\lambda)\, v_2^-(\lambda_n)\, v_3^+(\lambda)\,(\lambda+\lambda_n)} \tag{53}$$

with L_w, L_s, $v^{\pm}$, etc. as defined in (34), (35) and (31), (32).

Substituting (4), (29), (30), (51) and (33) into (53) and setting $\delta = 0$ we have

$$P_n^e(\lambda) \;=\; \left[\frac{-A(\lambda_n)}{\sqrt{1-\lambda_n^2}}\right] \frac{L_w(\lambda)\, L_w(\lambda_n)}{4\pi j L_s(\lambda)\, L_s(\lambda_n)} \frac{\sqrt{1-\lambda}\sqrt{1-\lambda_n}}{\lambda+\lambda_n} \tag{54}$$

$$P_n^h(\lambda) \;=\; B(\lambda_n) \frac{L_w(\lambda)\, L_w(\lambda_n)}{4\pi j L_s(\lambda)\, L_s(\lambda_n)} \frac{\sqrt{1+\lambda}\sqrt{1+\lambda_n}}{\lambda+\lambda_n} \tag{55}$$

corresponding to the spectra for the E_z and H_z polarizations, respectively. The modal field reflected back into the guide may be computed by substituting (52), (21) and (33) into (24) and employing the usual transformation to the λ plane to obtain

$$F_z^s \;=\; \int_{-\infty}^{\infty} \left[\frac{-v_4 v_3^-(\lambda_n)}{4\pi j\cos\left(k_o\delta\sqrt{1-\lambda_n^2}\right) v_2^-(\lambda)\, v_2^-(\lambda_n)\, v_3^+(\lambda)\,(\lambda+\lambda_n)}\right] \cdot \frac{L_w(\lambda_n;\delta)\; e^{-jk_o\delta\sqrt{1-\lambda^2}}}{L_s(\lambda)\, L_s(\lambda_n)\, U_w(\lambda;\delta)}$$

$$\cdot \left[2jA(\lambda)\frac{\sin\left(k_o y\sqrt{1-\lambda^2}\right)}{\sqrt{1-\lambda^2}} + 2B(\lambda)\cos\left(k_o y\sqrt{1-\lambda^2}\right)\right] e^{-jk_o x\lambda} d\lambda \quad ;\; 0 < y < \delta \tag{56}$$

As in the case of coupling, this integral can again be evaluated by closing the path

of integration in (56) via a semi-infinite contour in the lower half λ-plane to obtain

$$F^s_{zm} = \sum_{m=1}^{N} R_{mn} \left\{ jA(\lambda_m) \frac{\sin\left(k_o y\sqrt{1-\lambda_m^2}\right)}{\sqrt{1-\lambda_m^2}} + B(\lambda_m)\cos\left(k_o y\sqrt{1-\lambda_m^2}\right) \right\} e^{-jk_o x\lambda_m} \tag{57}$$

where R_{mn} are the mode reflection coefficients given by

$$R_{mn} = \frac{v_4 v_3^-(\lambda_n)\, e^{-jk_o\delta\sqrt{1-\lambda_m^2}}}{\cos\left(k_o\delta\sqrt{1-\lambda_n^2}\right) v_2^-(\lambda_m)\, v_2^-(\lambda_n)\, v_3^+(\lambda_m)\,(\lambda_m+\lambda_n)} \frac{L_w(\lambda_n;\delta)}{L_s(\lambda_m)\, L_s(\lambda_n)\, U_w'(\lambda_m;\delta)}. \tag{58}$$

When δ is set to zero, this reduces to

$$R^e_{mn} = \frac{A(\lambda_n)}{\sqrt{1-\lambda_n^2}} \frac{L_w(\lambda_n)}{L_s(\lambda_m)\, L_s(\lambda_n)\, U_w'(\lambda_m)} \frac{\sqrt{1-\lambda_m}\sqrt{1-\lambda_n}}{\lambda_m+\lambda_n} \tag{59}$$

$$R^h_{mn} = B(\lambda_n) \frac{L_w(\lambda_n)}{L_s(\lambda_m)\, L_s(\lambda_n)\, U_w'(\lambda_m)} \frac{\sqrt{1+\lambda_m}\sqrt{1+\lambda_n}}{\lambda_m+\lambda_n} \tag{60}$$

for the E_z and H_z polarizations, respectively.

5 Computation of Spectra for Material Insert in a Perfectly Conducting Ground Plane

We now have all the necessary components required for constructing the spectra P^e_{rs} associated with the multilayer slab recessed in a ground plane as defined in (14). Substituting (40), (46), (54), (59) and (11) into (14) we obtain the E_z polarization result

$$P^e_{rs}(\lambda,\lambda_o) = \frac{L_w(\lambda)\, L_w(\lambda_o)}{2\pi j L_s(\lambda)\, L_s(\lambda_o)} \frac{\sqrt{1-\lambda}\sqrt{1-\lambda_o}}{\lambda+\lambda_o} \left[1 + \sum_{m=1}^{N}\sum_{n=1}^{N} \frac{\tilde{V}^e_{mn}}{\lambda_o+\lambda_n} \left(\frac{\lambda+\lambda_o}{\lambda+\lambda_m} \right) \right] \tag{61}$$

where

$$\tilde{V}^e_{mn} = \frac{-A(\lambda_m)}{\sqrt{1-\lambda_m^2}} \frac{L_w(\lambda_m)}{L_s(\lambda_m)\, L_s(\lambda_n)\, U_w'(\lambda_n)} \sqrt{1-\lambda_m}\sqrt{1-\lambda_n} V^e_{mn} \tag{62}$$

$$V^e_{mn} = \{[I]_- + [R_{mn}]\}^{-1}_{mn}. \tag{63}$$

For H_z polarization, the spectra may be obtained by substituting (41), (47), (55), (60) and (11) into (14) to find

$$P^h_{rs}(\lambda, \lambda_o) = \frac{-L_w(\lambda)\, L_w(\lambda_o)}{2\pi j L_s(\lambda)\, L_s(\lambda_o)} \frac{\sqrt{1+\lambda}\sqrt{1+\lambda_o}}{\lambda+\lambda_o} \left[1 + \sum_{m=1}^{N}\sum_{n=1}^{N} \frac{\tilde{V}^h_{mn}}{\lambda_o+\lambda_n}\left(\frac{\lambda+\lambda_o}{\lambda+\lambda_m}\right)\right] \tag{64}$$

where

$$\tilde{V}^h_{mn} = B(\lambda_m) \frac{L_w(\lambda_m)}{L_s(\lambda_m)\, L_s(\lambda_n)\, U'_w(\lambda_n)} \sqrt{1+\lambda_m}\sqrt{1+\lambda_n} V^h_{mn} \tag{65}$$

$$V^h_{mn} = \{[I] - [R_{mn}]\}^{-1}_{mn}. \tag{66}$$

Expressions (61) and (64) can now be substituted into (13) and the resulting integral can be evaluated by the method of steepest descents to yield the far zone non-uniform diffracted field

$$F^s(\cos\phi, \cos\phi_o) \sim \sqrt{\frac{2\pi}{k_o}} e^{j\pi/4} P_{rs}(\cos\phi, \cos\phi_o) \frac{e^{-jk_o\rho}}{\sqrt{\rho}}, \tag{67}$$

where (ρ, ϕ) denote the usual cylindrical coordinates. In (67), F^s and P_{rs} refer to E^s_z and P^e_{rs} in the case of E_z incidence and to $Z_o H^s_z$, P^h_{rs} for H_z polarization. Although not apparent, (67) is reciprocal with respect to $\cos\phi$ and $\cos\phi_o$, as it should. We also note that $P_{rs}(\lambda, \lambda_o)$ is a combination of an inhomogeneous solution (direct diffracted term) and a sum of homogeneous solutions (modal contribution). It may also be easily shown from the asymptotic behavior of (61) and (64) that the homogeneous terms do not affect the edge condition.

6 Specialization to the GIBC Representation

To obtain numerical results, we must first provide expressions for the multilayered grounded slab reflection coefficient (i.e. $A(\lambda)$ and $B(\lambda)$), as well as the associated split functions and corresponding complex roots (waveguide modes). To accomplish these tasks in a simple manner, we consider the general GIBC approximation to $R(\lambda)$. This amounts to setting

$$\begin{aligned} A(\lambda) &= \sum_{n=0}^{N_A} A_n \left(1-\lambda^2\right)^n \\ B(\lambda) &= \sum_{n=0}^{N_B} B_n \left(1-\lambda^2\right)^n, \end{aligned} \tag{68}$$

where A_n and B_n are constants specific to the multilayered slab and are given in [Ricoy and Volakis, 1989b]. Introducing (68) into (21) yields

$$R(\lambda) = -\left[\frac{\sum_{n=0}^{N_A} A_n (1-\lambda^2)^n - \sqrt{1-\lambda^2}\sum_{n=0}^{N_B} B_n (1-\lambda^2)^n}{\sum_{n=0}^{N_A} A_n (1-\lambda^2)^n + \sqrt{1-\lambda^2}\sum_{n=0}^{N_B} B_n (1-\lambda^2)^n}\right] \tag{69}$$

and note that for a given order of approximation, N_A and N_B are finite and in general $N_A = N_B$ or $N_A = N_B + 1$, with the order of the condition equal to

$$N_S = max\,(2N_A, 2N_B + 1)\,. \tag{70}$$

To evaluate the split functions $L_w(\lambda;\delta)$ and $U_w(\lambda;\delta)$, (68) is substituted into (34) and by setting $\delta = 0$ we obtain

$$L_w(\lambda)\,U_w(\lambda) = \begin{cases} 2\sqrt{1-\lambda^2}\sum_{n=0}^{N_B} B_n (1-\lambda^2)^n & E_z \text{ polarization} \\ 2\sum_{n=0}^{N_A} A_n (1-\lambda^2)^n & H_z \text{ polarization.} \end{cases} \tag{71}$$

The split functions are then trivially obtained as

$$U_w(\lambda) = L_w(-\lambda) = \begin{cases} \sqrt{2B_{N_B}}\sqrt{1-\lambda}\prod_{n=1}^{N_B}\left[\sqrt{1-\xi_n}-\lambda\right] & E_z \text{ polarization} \\ \sqrt{2A_{N_A}}\prod_{n=1}^{N_A}\left[\sqrt{1-\xi_n}-\lambda\right] & H_z \text{ polarization,} \end{cases} \tag{72}$$

where $Im\sqrt{1-\xi_n} < 0$ and $\{\xi_n\}$ are the N_A zeros of $\sum_{n=0}^{N_B} B_n \chi^n$ for E_z polarization or $\sum_{n=0}^{N_A} A_n \chi^n$ for H_z polarization. It is apparent from (44) and (72) that the pertinent waveguide mode propagation constants are given by $k_0\sqrt{1-\xi_n}$.

In a similar fashion, we may substitute (68) into (35) to obtain

$$\begin{aligned} L_s(\lambda)\, U_s(\lambda) &= \sum_{n=0}^{N_A} A_n \sqrt{1-\lambda^2}^{\,2n} + \sum_{n=0}^{N_B} B_n \sqrt{1-\lambda^2}^{\,2n+1} \\ &= \sum_{n=0}^{N_S} S_n \sqrt{1-\lambda^2}^{\,n} \qquad (73) \\ &= S_0 \prod_{n=1}^{N_S} \left(1 + \frac{\sqrt{1-\lambda^2}}{\gamma_n}\right) \qquad (74) \end{aligned}$$

where

$$\begin{aligned} S_n &= \begin{cases} A_{n/2} & n \text{ is even} \\ B_{(n-1)/2} & n \text{ is odd,} \end{cases} \\ \{\gamma_n\} &= \{\text{zeros of the polynomial } \sum_{l=0}^{N_S} \frac{S_l}{S_0} (-1)^l \gamma^l\}. \qquad (75) \end{aligned}$$

The factorization of (74) is again trivial upon making use of the well known splitting germaine to the impedance half plane problem [*Senior*, 1952]. Noting that

$$1 + \eta\sqrt{1-\lambda^2} \stackrel{def}{=} \frac{1}{K_+(\lambda;\eta)\, K_-(\lambda;\eta)} \qquad (76)$$

we have,

$$U_s(\lambda) = L_s(-\lambda) = \frac{\sqrt{S_0}}{\prod_{n=1}^{N_S} K_+(\lambda; 1/\gamma_n)} \qquad (77)$$

where

$$K_+(\lambda;\eta) = K_-(-\lambda;\eta) = \begin{cases} \widetilde{K}_+(\lambda;\eta) & Re(\eta) \geq 0 \\ \left\{ j\eta \left(\lambda - \sqrt{1-1/\eta^2}\right) \widetilde{K}_+(\lambda;\eta) \right\}^{-1} & Re(\eta) < 0, \end{cases} \qquad (78)$$

and

$$\widetilde{K}_+(\cos\alpha;\eta) = \frac{\sqrt{\frac{8}{\eta}}\left[\Psi_\pi(3\pi/2-\alpha-\theta)\,\Psi_\pi(\pi/2-\alpha+\theta)\right]^2}{\Psi_\pi^4(\pi/2)\left[1+\sqrt{2}\cos\left(\frac{\pi/2-\alpha+\theta}{2}\right)\right]\left[1+\sqrt{2}\cos\left(\frac{3\pi/2-\alpha-\theta}{2}\right)\right]} \quad ; \quad Re(\eta \geq 0). \tag{79}$$

In the above $Im\left(\sqrt{1-1/\eta^2}\right) \leq 0$, $\theta = \sin^{-1}(\eta), 0 \leq Re(\theta)$, and Ψ_π is the Maliuzhinets function [*Maliuzhinets*, 1958], whose evaluation in algebraic form has been given in *Volakis and Senior* [1985]. Whereas the zeros of $U_w(\lambda)$ represent the waveguide modes, the zeros of $L_s(\lambda)$ (which are the poles of K_-) correspond to the surface waves supported by the material layer. Although not required in this analysis, these are easily extracted from (78) and (79).

The expressions (68) through (79) provide a complete description of a GIBC implementation and permit the simulation of any multilayered coating. We remark that a unique GIBC modeling of a given coating does not exist; in fact one may employ GIBCs of substantially different character to simulate the same configuration. This point is discussed in the following section and some numerical results are provided for illustration purposes.

7 Numerical Results

In this section GIBC simulations of various material inserts are presented and compared with exact results available for the case of a single layer. Due to its greater interest, data is presented only for the H_z polarization case. The GIBCs employed here-in are given in *Ricoy and Volakis* [1989b]. These are valid for arbitrary multilayer coatings and are therefore suited for this application. In particular, these multilayer GIBCs are synthesized by combining the component-layer GIBCs

in an appropriate manner, pointing to the necessity of understanding single layer simulations in order to construct multilayer ones.

Figure 3 shows the far zone pattern of a single layer insert ($\epsilon = 2 - j.0001, \mu = 1.2, \tau = .2\lambda$) modeled by various "low contrast" GIBCs (i.e. those GIBCs which improve as the layer thickness or index of refraction decreases). To illustrate their relative contributions to the far zone pattern, the direct diffraction and modal contributions have been isolated in figures 3a and 3b, respectively, with the overall result presented in figure 3c. We note that for this low contrast GIBC, an 8^{th} order simulation provides a reasonable approximation to the diffraction pattern.

In Figure 4, both the thickness and the index of refraction have been increased in a low contrast simulation of a (single layer) material insert with $\epsilon = 3.5 - j.0001, \mu = 2.0$, and $\tau = .4\lambda$. In contrast to the previous figure we now observe that a $20th$ order simulation is required to obtain a converged result. This degradation with increasing index of refraction proves typical of low contrast simulations and illustrates the need for other types of GIBCs whose performance improves in this range of material parameters.

In Figure 5 the same material insert corresponding to the data of figure 4 is simulated with high contrast GIBC (i.e., a GIBC which improves as the index of refraction increases or as the layer thickness decreases). In contrast to the data in figure 4, we now observe that only a second order high contrast GIBC simulation is required to accurately evaluate the far zone scattering. This difference in performance between the low and high contrast GIBCs stems from the type of approximation employed in their derivation and the reader is referred to *Ricoy*

and Volakis [1989b] for a more in depth discussion. Some insight on the type of simulation provided by the low and high contrast GIBCs may be gained through an examination of the waveguide modes predicted by the different simulations. These are presented in Tables 1 and 2 for the single layer simulations corresponding to the data in figures 4 and 5. The exact modes given in the table are generated by the equation

$$\lambda_n = \sqrt{\epsilon_r \mu_r - \left(\frac{n\pi}{k_0 \tau}\right)^2}, \quad n = 0, 1, 2, \ldots. \tag{80}$$

We observe that as the order of the low contrast simulation is increased, the data in table 1 reveal that the waveguide modes are "picked up" in a sequential manner corresponding to increasing n in (80). On the other hand (see table 2), the high contrast GIBCs pick up the $n = 2$ exact mode immediately and then "branch off" to pick up the other modes. The discrepency in pattern convergence between figures 4 and 5 clearly suggests that the $n = 2$ mode is the most significant in terms of diffraction (for this particular configuration). We explain this physically by noting that the $n = 2$ mode may be resolved into its constituent rays which strike the interface at a characteristic angle (say θ_2^{mod}) which is greater than the critical angle θ^c of the material insert. On the other hand, the $n = 0$ and $n = 1$ modes are associated with characteristic angles less than the critical angle. This implies that upon coupling into the slab, the $n = 2$ waveguide mode is partially transmitted into free space while the lower order waveguides modes remain bound.

The above hypothesis may be tested by computing exact solutions in which the selection of the included waveguide modes parallels the order in which they are picked up depending on whether a low or high contrast GIBC simulation is

employed. Figure 6 depicts a high contrast simulation of a single layer having $\epsilon = 11 - j.0001, \mu = 7$, and $\tau = .4\lambda$. The 10-mode result is a pattern obtained by adding in modes sequentially as determined from (80), thus paralleling a low contrast mode selection scheme. On the other hand, the single mode result contains the contribution of only the $n = 7$ mode (the mode with $\theta^m > \theta^c$), thus, paralleling the high contrast mode selection criteria. This clearly verifies that the most significant waveguide modes are those that are "visible", i.e. those with $\theta^m > \theta^c$.

Finally, figure 7 provides a simulation of a three layer insert composed of two high contrast layers ($\epsilon = 11 - j.0001, \mu = 7$, and $\tau = .4\lambda$ and $\epsilon = 3.5 - j.0001, \mu = 2.0$, and $\tau = .4\lambda$) placed beneath a low contrast layer with $\epsilon = 2 - j.0001, \mu = 1.2$ and $\tau = .2\lambda$. These are precisely the layers considered earlier in isolation. One might, therefore, expect that the order of the GIBC which provided converged results for the single layer simulation will also provide an equally acceptable simulation when the slab is part of the multilayer stack. For the case at hand this is indeed true, as evidenced by the converged 9^{th} order result. We also remark that the presence of the two high contrast layers enhances the modal contribution to the total diffraction when compared with the single layer data given in figures 3b and 3c.

8 Summary

In summary, the scattering from a vertically inhomogeneous slab recessed in a ground plane was obtained through application of the generalized scattering matrix technique in conjunction with the dual integral equation approach. The solution

was specialized to the case of a multilayered slab simulated with a generalized impedance boundary condition (GIBC). Results were given for various single layer inserts and it was seen that in the case of materials having sufficiently high index of refraction, high contrast GIBC simulations converged more rapidly (with respect to the order of the GIBC) and performed better than low contrast simulations. Finally, results were presented for a 1λ-thick lossless three-layer insert containing both high and low contrast layers. It was shown that the simulation converged at the point predicted by the individual layer simulations, suggesting a method for constructing multi-layer simulations.

References

Bernard, J. M. L., "Diffraction by Metallic Wedge Covered with a Dielectric Material," Journal of Wave Motion, Vol. 9, pp. 543-561, 1987.

Clemmow, P. C., "A method for the exact solution of a class of two-dimensional diffraction problems," Proc. Roy. Soc. A, Vol. 205, pp. 286-308, 1951.

Karp, S. N. and Karal Jr., F. C., "Generalized Impedance Boundary Conditions with Applications to Surface Wave Structures," in Electromagnetic Wave Theory, Part 1, ed. J. Brown, pp. 479-483, Pergamon: New York, 1965.

Maliuzhinets, G. D., " Excitation, Reflection and Emission Of Surface Waves From a Wedge With Given Face Impedances," *Sov. Phys. Dokl.*, Engl. Transl., 3, 752-755, 1958.

Pace, J. R. and Mittra, R., "Generalized scattering matrix analysis of waveguide discontinuity problems," Proc. Symp. Quasi-Optics, Vol. 14, Brooklyn, N.Y., Polytechnic Inst. of Brooklyn Press, pp. 177-197, 1964.

Pathak, P. H. and Kouyoumjian, R. G., "Surface wave diffraction by a truncated dielectric slab recessed in a perfectly conducting surface," Radio Science, Volume 14, Number 3, pp. 405-417, May-June 1979.

Ricoy, M. A. and Volakis, J. L., "E-polarization Diffraction by a thick metal-dielectric join," Journal of Electromagnetic Waves and Applications, No. 8, 1989a.

Ricoy, M. A. and Volakis, J. L., "Derivation of generalized transition/boundary conditions for planar multiple layer structures," submitted to Radio Science, 1989b.

Rojas, R. G., and Z. Al-hekail, "Generalized Impedance/Resistive Boundary Conditions for Electromagnetic Scattering Problems," Radio Science, Vol. 24, No. 1, pp. 1-12, Jan-Feb 1989.

Senior, T. B. A. and Volakis, J. L., "Derivation and Application of a Class of Generalized Boundary Conditions," IEEE Trans. on Antennas and Propagat., December, 1989 (in press).

Senior, T. B. A., "Diffraction by a semi-infinite metallic sheet, Proc. Roy. Soc. (London), A213,pp. 436-458, 1952.

Volakis, J. L. and Ricoy, M. A., "H-polarization Diffraction by a thick metal-dielectric join," IEEE Transactions on Antennas and Propagation, November, 1989 (in press).

Volakis, J. L., and Senior, T. B. A., "Application of a Class of Generalized Boundary Conditions to Scattering by a Metal-Backed Dielectric Half Plane," Proceedings of the IEEE, pp 796-805, May 1989.

Volakis, J. L., and Syed, H. H., "Application of Higher Order Boundary Conditions to Scattering by Multilayered Coated Cylinders," University of Michigan Radiation Laboratory Report 389757-2-T, 1989.

Volakis, J. L. and Senior, T. B. A.,"Simple expressions for a function occurring in diffraction theory," *IEEE Trans. Antennas Propag.*, vol. AP-33, pp. 678-680, June 1985.

Table Captions

Table 1. Low contrast approximation to waveguide modes for a layer with $\epsilon = 3.5 - j.0001, \mu = 2.0$, and $\tau = .4\lambda$. For each low contrast boundary condition, the three numbers of the column headings indicate the order of the approximation in thickness τ, the order of the resulting boundary condition, and the total number of modes (see [Ricoy and Volakis, 1989b]).

Table 2. High contrast approximation to waveguide modes for a layer with $\epsilon = 3.5 - j.0001, \mu = 2.0$, and $\tau = .4\lambda$. For each high contrast boundary condition, the three numbers of the column headings indicate the approximation in the index of refraction κ^{-1}, the order of the resulting boundary condition, and the total number of modes.

Table 1: Low contrast approximation to waveguide modes for a layer with $\epsilon = 3.5 - j.0001, \mu = 2.0$, and $\tau = .4\lambda$. For each low contrast boundary condition, the three numbers of the column headings indicate the order of the approximation in thickness τ, the order of the resulting boundary condition, and the total number of modes (see [Ricoy and Volakis, 1989b]).

Exact Modes	L. C.(1,2,1)	L.C.(5,6,3)	L.C.(9,10,5)	L.C.(13,14,7)	L.C.(17,18,9)	L.C.(21,22,11)
$2.6458 - j0$	$2.6458 - j0$	$2.6458 - j0$	$2.6458 - j0$	$2.6458 - j0$	$2.6458 - j0$	$2.6458 - j0$
$2.3318 - j0$		$2.3324 - j.1518$	$2.3303 - j0$	$2.3318 - j0$	$2.3318 - j0$	$2.3318 - j0$
$0.8660 - j0.0001$		$-2.3324 - j.1517$	$1.7608 - j.0001$	$1.1583 - j.0001$	$0.8782 - j.0001$	$0.86612 - j.0001$
$0 - j2.6575$			$2.3156 - j.1518$	$1.5228 - j1.4058$	$0.8198 - j1.9935$	$0.3937 - j2.6289$
$0 - j4.2464$			$-2.3156 - j.1517$	$-1.5227 - j1.4058$	$-0.8197 - j1.9934$	$-0.3936 - j2.6289$
$0 - j5.6624$				$3.0782 - j2.1345$	$2.2444 - j2.6318$	$1.6576 - j3.1906$
$0 - j7.0178$				$-3.0782 - j2.1344$	$-2.2444 - j2.6318$	$-1.6576 - j3.1906$
$0 - j8.3404$					$4.1090 - j2.8858$	$3.1642 - j3.5300$
$0 - j9.6437$					$-4.1090 - j2.8858$	$-3.1642 - j3.5300$
$0 - j10.9348$						$5.2491 - j3.5008$
$0 - j12.2168$						$-5.2491 - j3.5008$

Table 2: High contrast approximation to waveguide modes for a layer with $\epsilon = 3.5 - j.0001, \mu = 2.0$, and $\tau = .4\lambda$. For each high contrast boundary condition, the three numbers of the column headings indicate the approximation in the index of refraction κ^{-1}, the order of the resulting boundary condition, and the total number of modes.

Exact Modes	H. C.(0,2,1)	H.C.(1,4,2)	H.C.(2,6,3)	H.C.(3,8,4)	H.C.(4,10,5)
$2.6458 - j0$				$7.9636 - j.0032$	$3.2862 - j.0001$
$2.3318 - j0$		$5.5825 - j.0023$	$2.2571 - j.0001$	$2.2813 - j0$	$2.2714 - j0$
$0.8660 - j0.0001$	$0.8667 - j.0001$	$0.8649 - j.0001$	$0.8660 - j.0001$	$0.8660 - j.0001$	$0.8660 - j.0001$
$0 - j2.6575$			$0 - j2.1309$	$0 - j2.0694$	$0.6002 - j2.2920$
$0 - j4.2464$					$-0.6002 - j2.2920$

Figure Captions

Figure 1. (a) Multilayer slab recessed in PEC groundplane.
(b) Representation of slab as surface with reflection coefficient R.

Figure 2. Illustration of recessed stub geometry (a) and associated subproblems: (b) direct diffraction, (c) mode coupling, (d) stub reflection, (e) mode reflection at waveguide mouth, (f) mode launching.

Figure 3. H_z polarization backscatter echo width for a material insert with $\tau = .2\lambda$, $\epsilon = 2 - j.0001$, $\mu = 1.2$ modeled by low contrast GIBCs (See Table 1 for an explanation of the legend entries). (a) Direct diffraction component. (b) Modal component. (c) Composite.

Figure 4. H_z polarization backscatter echo width for a material insert with $\tau = .4\lambda$, $\epsilon = 3.5 - j.0001$, $\mu = 2$ modeled by low contrast GIBCs (See Table 1 for an explanation of the legend entries). (a) Direct diffraction component. (b) Modal component. (c) Composite.

Figure 5. H_z polarization backscatter echo width for a material insert with $\tau = .4\lambda$, $\epsilon = 3.5 - j.0001$, $\mu = 2$ modeled by high contrast GIBCs (See Table 2 for an explanation of the legend entries). (a) Direct diffraction component. (b) Modal component. (c) Composite.

Figure 6. H_z polarization backscatter echo width for a material insert with $\tau = .4\lambda$, $\epsilon = 11. - j.0001$, $\mu = 7$ modeled with high contrast GIBCs (See Table 2 for an explanation of the legend entries).

Figure 7. H_z polarization backscatter echo width for a three-layer material insert with ($\tau_1 = .4\lambda$, $\epsilon_1 = 11. - j.0001$, $\mu_1 = 7.$), ($\tau_2 = .4\lambda$, $\epsilon_2 = 3.5 - j.0001$, $\mu_2 = 2$), ($\tau_3 = .2\lambda$, $\epsilon_3 = 2 - j.0001$, $\mu_3 = 1.2$). In the legend entry $a, b, c(d, e)$, a and b denote the approximation in κ^{-1} of the high contrast layers 1 and 2, c denotes the approximation in τ of the low contrast layer 3, while d is the order of the composite GIBC and e is the total number of modes.

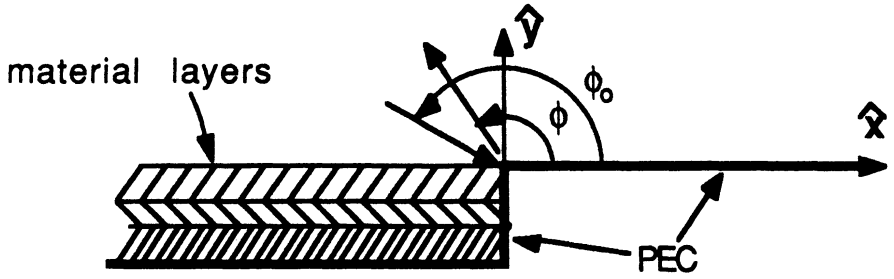

(a)

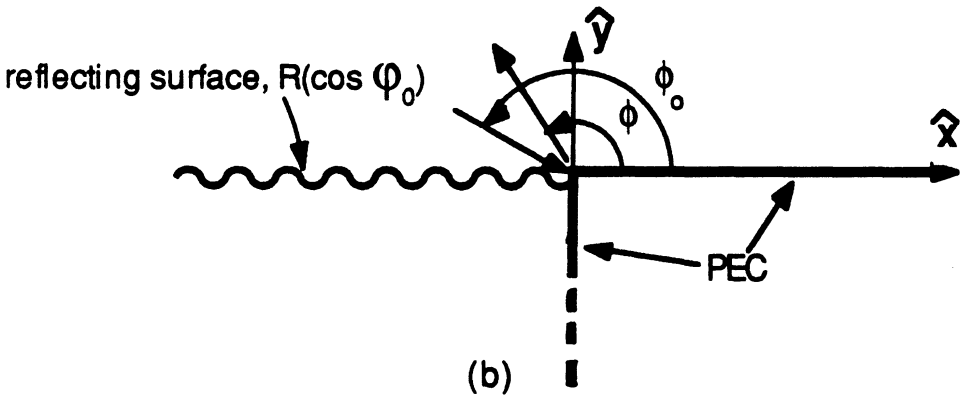

(b)

Figure 1. (a) Multilayer slab recessed in PEC groundplane.
(b) Representation of slab as surface with reflection coefficient R.

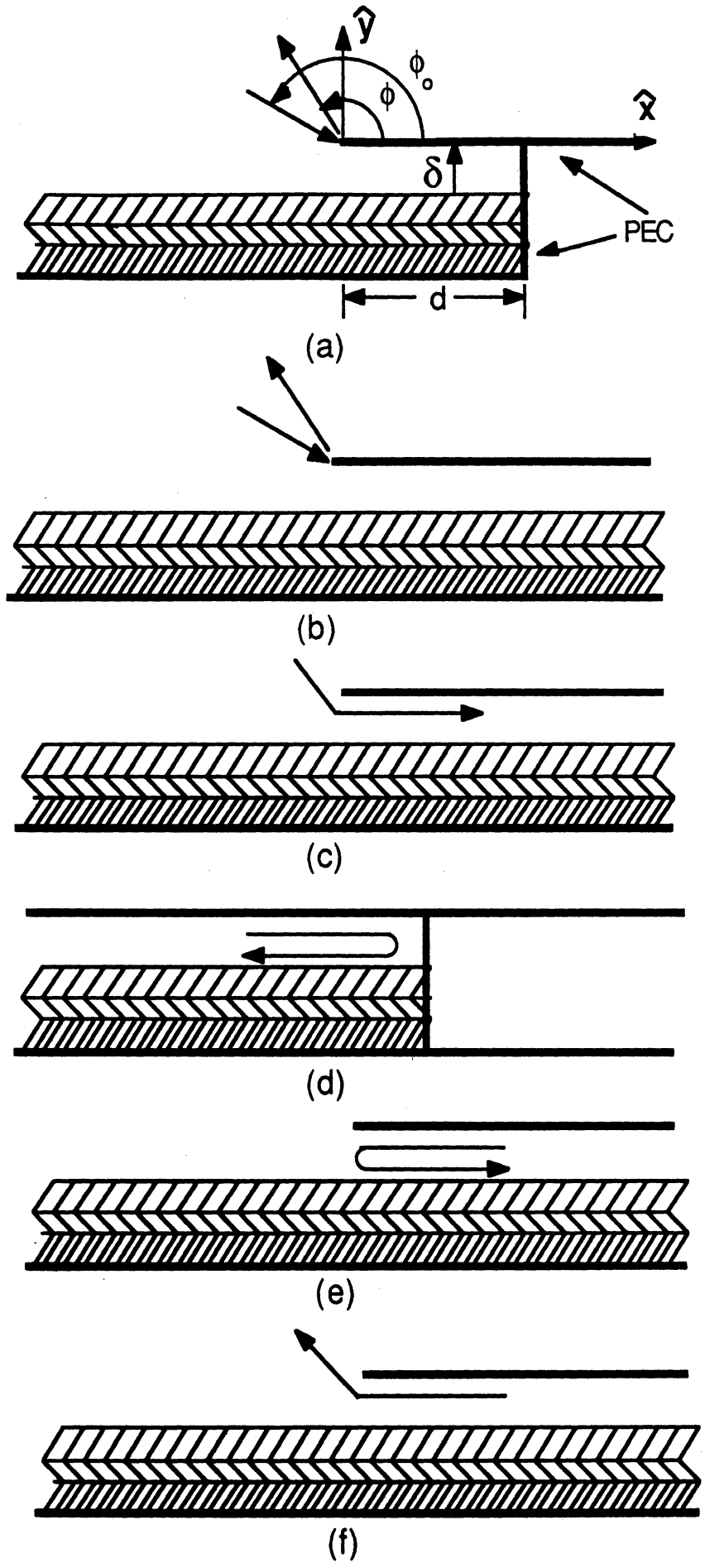

Figure 2. Illustration of recessed stub geometry (a) and associated suproblems: (b) direct diffraction, (c) mode coupling, (d) stub reflection, (e) mode reflection at waveguide mouth, (f) mode launching.

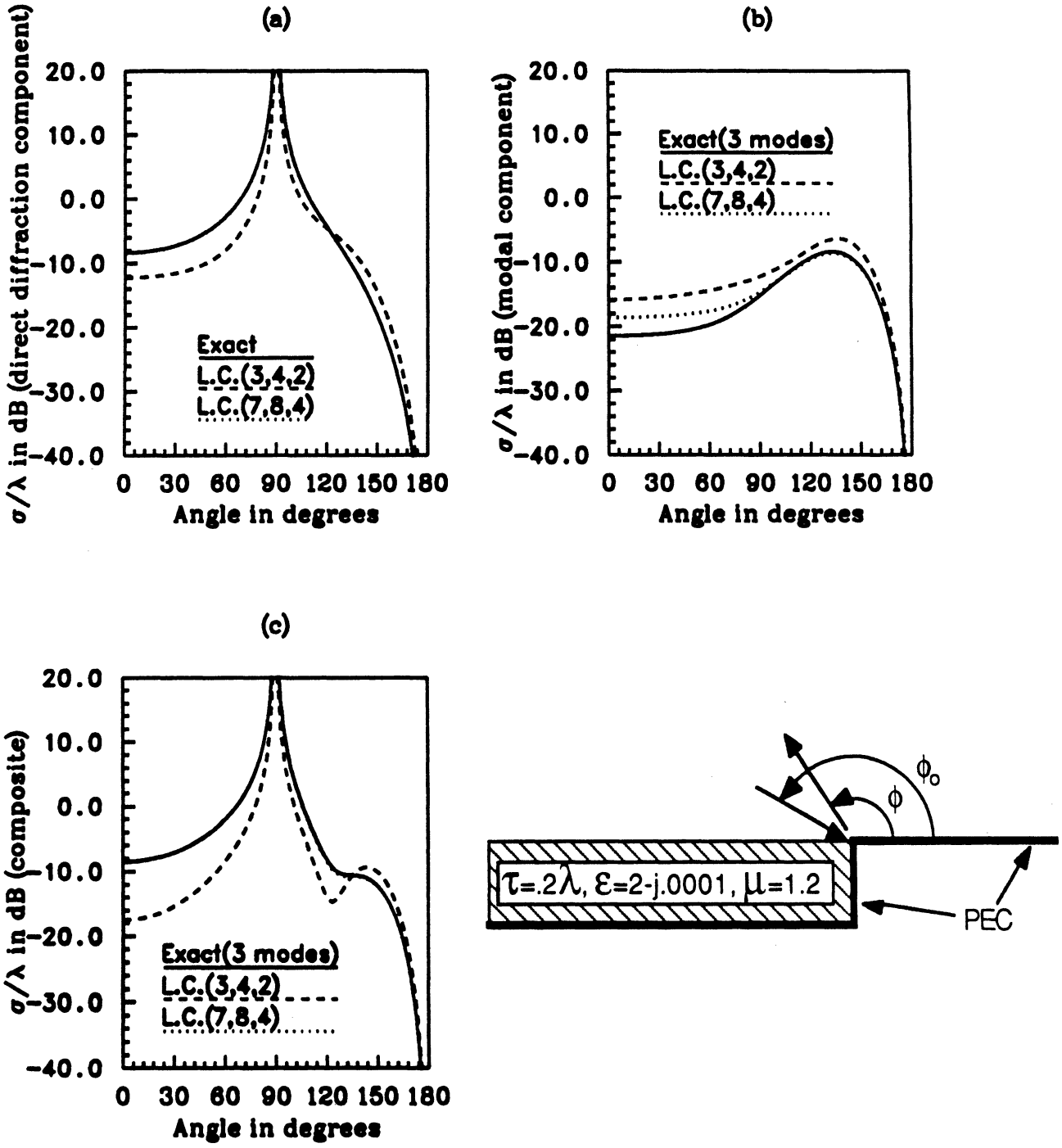

Figure 3. H_z-polarization backscatter echo width for a material insert with τ=.2λ, ε=2-j.0001, μ=1.2 modeled by low contrast GIBCs (See Table 1 for an explanation of the legend entries). (a) Direct diffraction component. (b) Modal component. (c) Composite.

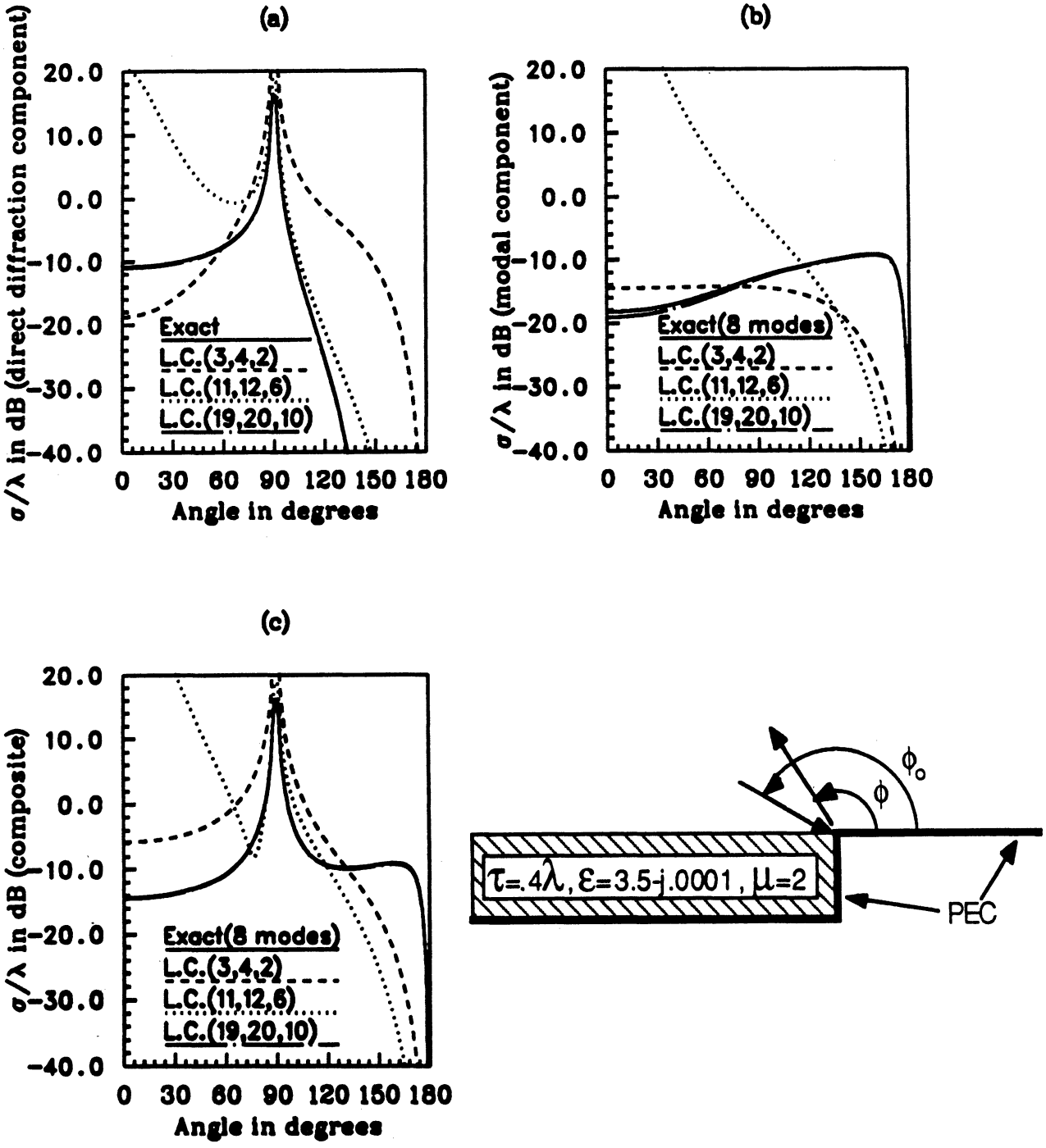

Figure 4. H_z-polarization backscatter echo width for a material insert with $\tau=.4\lambda$, $\varepsilon=3.5-j.0001$, $\mu=2$ modeled by low contrast GIBCs (See Table 1 for an explanation of the legend entries). (a) Direct diffraction component. (b) Modal component. (c) Composite.

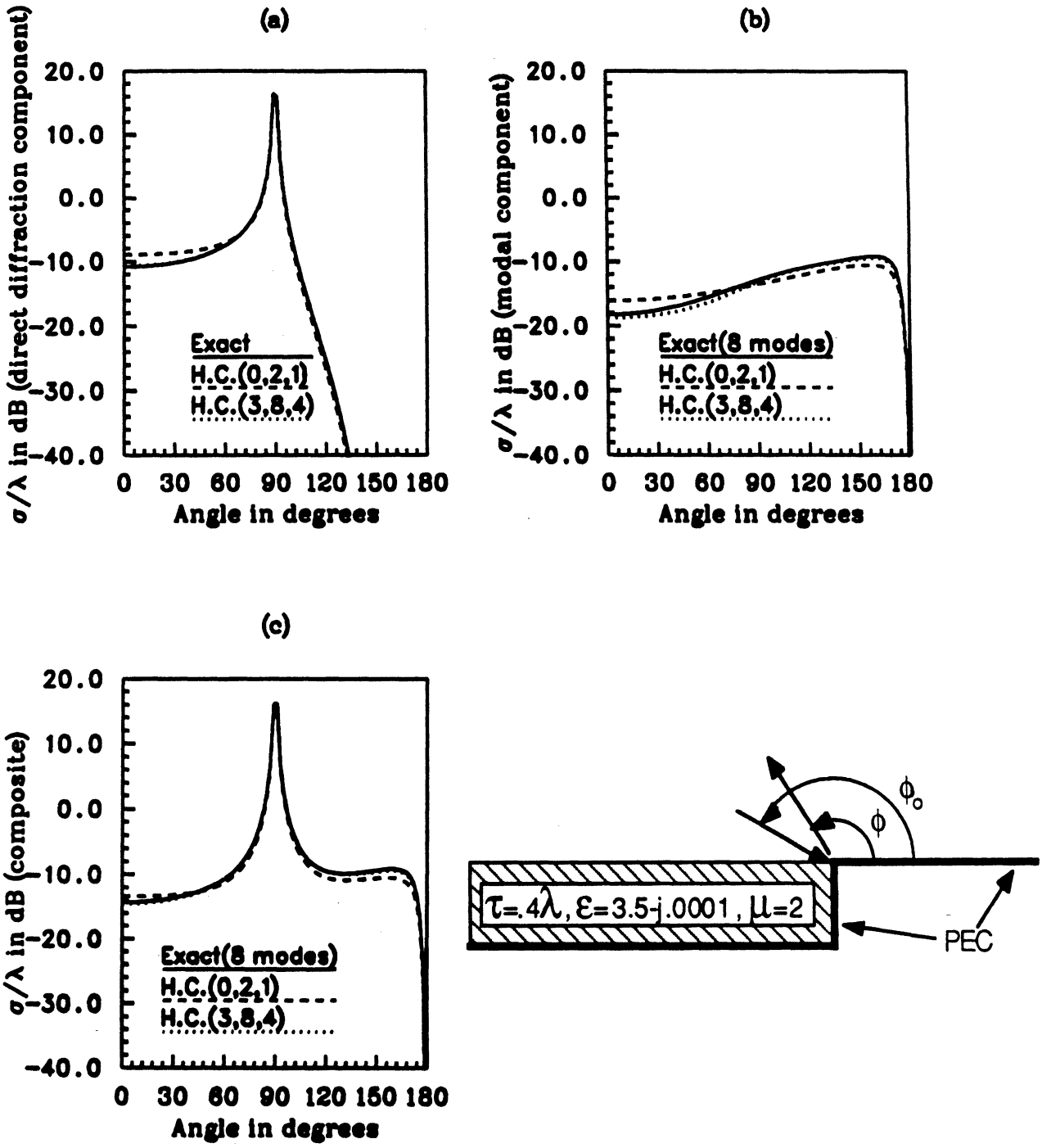

Figure 5. H_z-polarization backscatter echo width for a material insert with $\tau=.4\lambda$, $\varepsilon=3.5-j.0001$, $\mu=2$ modeled by high contrast GIBCs (See Table 2 for an explanation of the legend entries). (a) Direct diffraction component. (b) Modal component. (c) Composite.

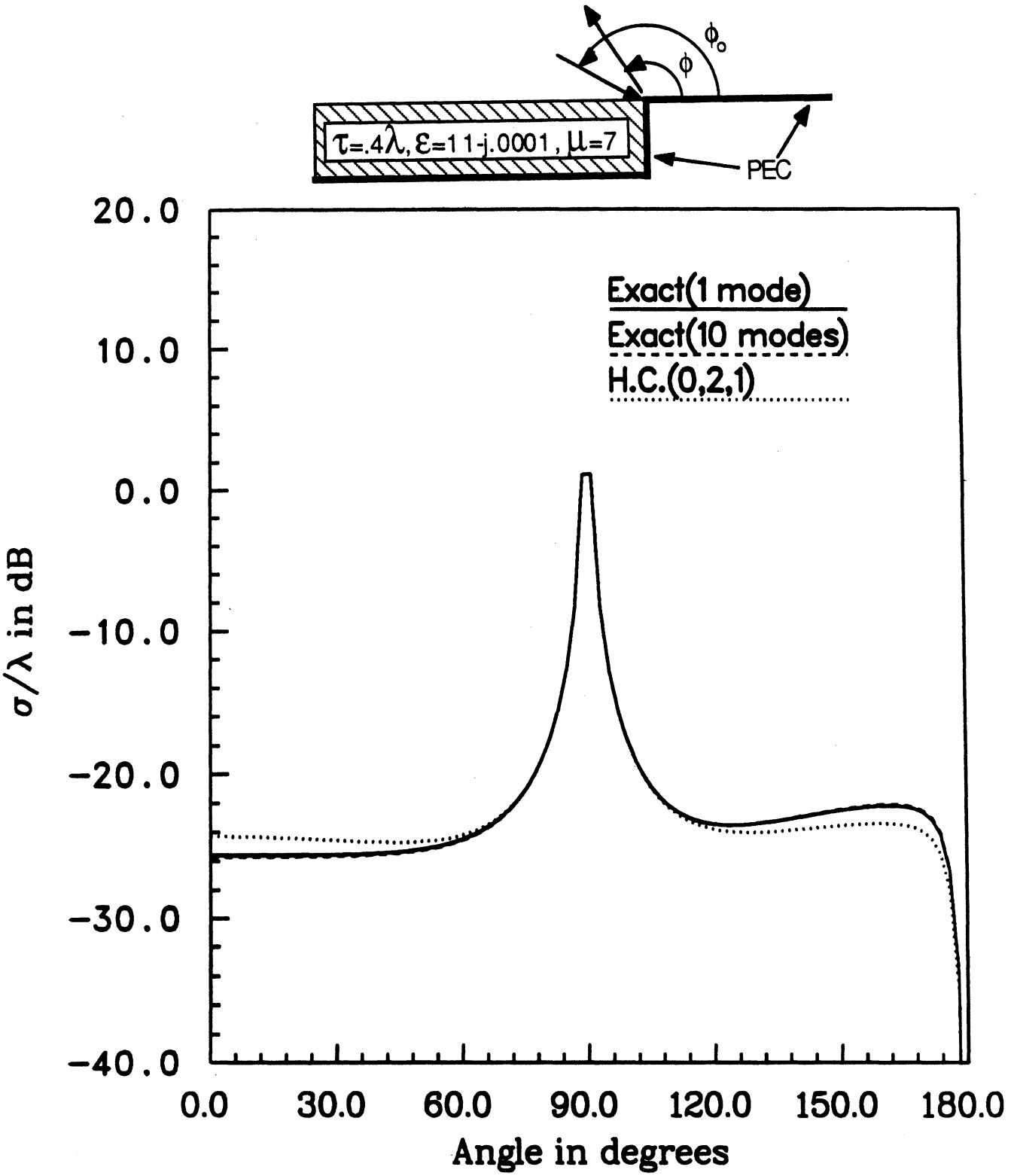

Figure 6. H_z-polarization Backscatter echo width for material insert with τ=.4λ,ε=11-j.0001, μ=7 modeledwith high contrast GIBCs (see Table 2 for an explanation of the legend entries).

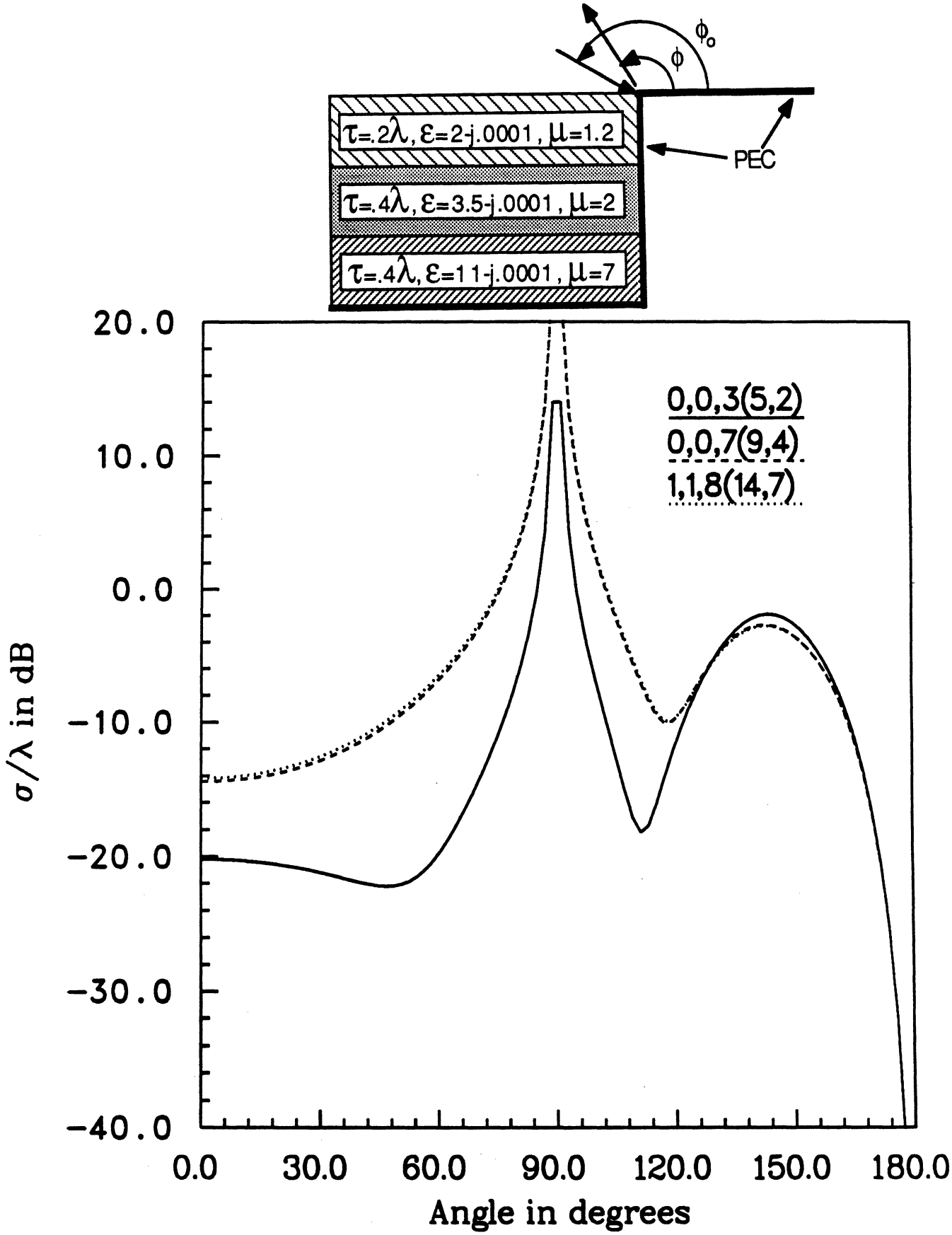

Figure 7. H_z-polarization Backscatter echo width for a three-layer material insert with (τ_1=.4λ, ε_1=11-j.0001, μ_1=7), (τ_2=.4λ, ε_2=3.5-j.0001, μ_2=2), (τ_3=.2λ, ε_3=2-j.0001, μ_3=1.2). In the legend entry a,b,c(d,e), a and b denote the approximation in κ^{-1} of the high contrast layers 1 and 2, c denotes the approximation in τ of the low contrast layer 3, while d is the order of the composite GIBC and e is the total number of modes.